Title

Optimized Negative Staining: a High-throughput Protocol for Examining Small and Asymmetric Protein Structure by Electron Microscopy

Authors

Rames, Matthew

Yu, Yadong

Ren, Gang

Publication Date

2014

DOI

10.3791/51087

Peer reviewed

Video Article

Optimized Negative Staining: a High-throughput Protocol for Examining Small and Asymmetric Protein Structure by Electron Microscopy

Matthew Rames[1], Yadong Yu[1], Gang Ren[1]

[1]Lawrence Berkeley National Laboratory, The Molecular Foundry

Correspondence to: Gang Ren at gren@lbl.gov

URL: http://www.jove.com/video/51087
DOI: doi:10.3791/51087

Keywords: Environmental Sciences, Issue 90, small and asymmetric protein structure, electron microscopy, optimized negative staining

Date Published: 8/15/2014

Citation: Rames, M., Yu, Y., Ren, G. Optimized Negative Staining: a High-throughput Protocol for Examining Small and Asymmetric Protein Structure by Electron Microscopy. *J. Vis. Exp.* (90), e51087, doi:10.3791/51087 (2014).

Abstract

Structural determination of proteins is rather challenging for proteins with molecular masses between 40 - 200 kDa. Considering that more than half of natural proteins have a molecular mass between 40 - 200 kDa[1,2], a robust and high-throughput method with a nanometer resolution capability is needed. Negative staining (NS) electron microscopy (EM) is an easy, rapid, and qualitative approach which has frequently been used in research laboratories to examine protein structure and protein-protein interactions. Unfortunately, conventional NS protocols often generate structural artifacts on proteins, especially with lipoproteins that usually form presenting rouleaux artifacts. By using images of lipoproteins from cryo-electron microscopy (cryo-EM) as a standard, the key parameters in NS specimen preparation conditions were recently screened and reported as the optimized NS protocol (OpNS), a modified conventional NS protocol [3] . Artifacts like rouleaux can be greatly limited by OpNS, additionally providing high contrast along with reasonably high#resolution (near 1 nm) images of small and asymmetric proteins. These high-resolution and high contrast images are even favorable for an individual protein (a single object, no average) 3D reconstruction, such as a 160 kDa antibody, through the method of electron tomography[4,5]. Moreover, OpNS can be a high#throughput tool to examine hundreds of samples of small proteins. For example, the previously published mechanism of 53 kDa cholesteryl ester transfer protein (CETP) involved the screening and imaging of hundreds of samples [6]. Considering cryo-EM rarely successfully images proteins less than 200 kDa has yet to publish any study involving screening over one hundred sample conditions, it is fair to call OpNS a high-throughput method for studying small proteins. Hopefully the OpNS protocol presented here can be a useful tool to push the boundaries of EM and accelerate EM studies into small protein structure, dynamics and mechanisms.

Video Link

The video component of this article can be found at http://www.jove.com/video/51087/

Introduction

Understanding protein function requires knowledge of protein structure. Structural determination is challenging for proteins whose molecular masses are within 40 - 200 kDa. X-ray crystallography is limited by protein crystallization; nuclear magnetic resonance (NMR) spectroscopy is limited to molecular masses less than 40 KDa, while cryo-electron microscopy (cryo-EM) has difficulty in both image acquisition and three-dimensional (3D) reconstructions of small proteins, which molecular masses are less than 200 kDa. Notably, more than 50% proteins have a molecular mass within the range of 40 - 200 kDa[1,2], as current methods are challenging in studying proteins of this size, a new method is needed.

Although most transmission electron microscopes (TEMs) are capable of atomic resolution, *i.e.,* better than 3 Å resolution, achieving even a near nanometer resolution structure from a biological samples is rather challenging[7]. Radiation damage, low contrast, structural deviations as well as artifacts such as dehydration all hinder high-resolution TEM imaging[3,8].

Among various TEM approaches, cryo-EM is an advanced and cutting edge method to achieve atomic resolution structures of highly symmetric large macromolecules under near physiological conditions[9-12]. The cryo-EM sample is prepared flash freezing the sample solution, embedding the macromolecules in vitreous ice, which is subsequently imaged at cryogenic temperatures such as liquid nitrogen or helium temperatures[13]. Cryo-EM is advantageous in that samples present no artifacts and are nearly native in structure[8-12]. Cryo-EM does have its disadvantages: i) additional devices are required to be installed or purchased to upgrade a standard TEM instrument for a cryo-EM capability. Devices include: anti-contaminator, cryo-holder, low-dose mode software and low-dose sensitive CCD camera, although the prices of these devices are much lower than the price of the TEM instrument itself; ii) cryo-EM operation needs longer time than NS operation. Examining a cryo-EM specimen often requires longer time to prepare specimens and operate the TEM instrument than that of NS because cryo-EM requires addressing additional difficulties, including: liquid nitrogen temperature operation, sample charging, imaging drift, temperature gradients, low-dose model operation, sample radiation sensitivities and dosage limitations. These extra steps will slow down the speed of acquiring useful data compared to NS data acquisition, although a few cryo-EM images can certainly be obtained in 1 hr or less by cryo-EM experts with the instrument prepared with a balanced temperature gradient; iii) users require additional training, such as handling liquid nitrogen, freezing cryo-EM grids, low-dose operation, dose measurement, handling the charging, drifting and knowledge in imaging processing; iv) lack of repeatable imaging for the same

cryo-specimen during different TEM sessions. Cryo-EM specimens are easily damaged by ice contamination during specimen loading and unloading to/from the TEM instrument. This damage is especially a concern when the samples are difficult to be isolated/purified[14]; v) small proteins (<200 kDa molecular mass) are challenging to be imaged because of low contrast; vi) the low contrast and high noise of cryo-EM images reduces the cross-correlation value between images, therefore, decreasing overall accuracy in the determination of protein orientations, conformations and classifications, especially for proteins that are structurally flexible and naturally fluctuate in solution[4,5].

Negative staining (NS) is a relatively "ancient" and historical method which any laboratory, with any type EM, can utilize to examine protein structure. Brenner and Horne first developed the concept of negative staining a half century ago for examining viruses[15]. NS is accomplished through coating the specimen with charged heavy metal salts. This concept originally coming from light microscopy and the practice of embedding bacteria into a stain solution providing darkness around the specimens, allowing higher image contrast when viewing the negative image[16]. Since the heavy metal ions have a greater ability to disperse electrons compared to less dense atoms in the proteins[17-20], and coating heavy metal stain permits a higher dosage limitation with improved contrast. NS specimen can provide high contrast images[8] for easier particle orientation determination and 3D reconstruction than images from cryo-EM.

Traditional NS, unfortunately, can produce artifacts induced by stain-protein interactions, such as general aggregation, molecular dissociation, flattening and stacking[8,21,22]. For lipid related proteins, such as lipoproteins[16,23-30], a common artifact results in particles that are stacked and packed together into a rouleaux (**Figure 1**)[31-36]. Many lipoprotein studies, such as nondenaturing polyacrylamide gradient gel electrophoresis, cryo-EM studies[13,29,37-40], mass spectrometry[39,41], and small angle X-ray diffraction data[42] all show lipoprotein particles are isolated particles instead of naturally stacked together forming a rouleaux [21,29,30,35,42-45]. The observation of rouleaux formation by conventional NS is possibly caused by dynamic interactions between lipoproteins composed of apolipoproteins (apo) and phospholipids that are structurally flexible in solution [13,29,30,46-49] and sensitivity to the standard NS protocol. To identify this artifact, apolipoprotein E4 (apoE4) palmitoyl-oleoylphosphatidylcholine (POPC) high-density lipoprotein (HDL) sample were used as a test sample and cryo-EM images for an artifact free standard [29], screening the NS specimens prepared under a series of conditions. By comparing the particle sizes and shapes obtained from NS and cryo-EM, the specific type of staining reagent and salt concentration were found to be two key parameters causing the well known rouleaux phenomena. Thus, an optimized negative staining (OpNS) protocol was reported.

By OpNS, the well known rouleaux phenomenon of apoE4 HDL was eliminated by OpNS (**Figure 2A**). Statistical analysis demonstrated OpNS yields very similar images (fewer than 5% deviation) in size and shape in comparison to those from cryo-EM, however the contrast was eliminated. The validations of OpNS were performed by examining the elimination of the rouleaux artifact of nearly all classes or subclasses of lipoprotein samples [6,29,30,50,51], including apoA-I 7.8 nm (**Figure 2B**), 8.4 nm (**Figure 2C**), 9.6 nm discoidal reconstituted HDL (rHDL) (**Figure 2D**), 9.3 nm spherical rHDL (**Figure 2E**), human plasma HDL (**Figure 2F**), lipid free apoA-I (**Figure 2G**), plasma HDL (**Figure 2H**), low density lipoprotein (LDL) (**Figure 2I**), intermediate#density lipoprotein (IDL) (**Figure 2J**), very low density lipoprotein (VLDL) (**Figure 2K**), and POPC liposome (**Figure 2L**) [30]. Additional validations were performed by imaging small and asymmetric proteins, including the 53 kDa cholesteryl ester transfer protein (CETP) (**Figure 3A** - **C**)[6,29], and highly flexible 160 kDa IgG antibody (**Figure 4A** and **B**)[4,5,29,52], and two structurally well known proteins, GroEL and proteasome (**Figure 2M** and **N**). For requiring any additional validation from colleagues, we are open to any blind tests on this OpNS method.

OpNS as a high-throughput protocol has also been used to study protein mechanism via examining hundreds of samples of small proteins, such as CETP that was binding to various proteins under a series conditions (including CETP interacting to 4 classes of lipoproteins, recombined HDL, plasma HDL, LDL and VLDL, with/without 2 antibodies, H300 and N13, under 9 incubation times, including 3 min, 20 min, 1 hr, 2 hr, 4 hr, 8 hr, 24 hr, 48 hr and 72 hr, under 4 molar ratios, *i.e.,* 1:0.5, 1:1, 1:2, 1:4, and 3 dilutions, *i.e.,* 0.1 mg/ml, 0.01 mg/ml and 0.001 mg/ml, plus additional control samples, including CETP alone, LDL alone, and VLDL alone, with triple tests of above experiments by different persons)[6,29]. OpNS images of CETP provided high contrast images with reasonably fine structural details; allowing us to successfully reconstruct a 3D density map of the 53 kDa small protein CETP (**Figure 3D** - **F**) by single particle reconstruction. Moreover, the high contrast OpNS images provide us a sufficient signal from an individual protein (**Figure 4A** - **C**), which allowed us to achieve the intermediate resolution (~1.5 nm) of a single (one object, no average) IgG antibody 3D structure via the individual-particle electron tomography (IPET) method (**Figure 4E** - **J**)[5]. The detailed description of IPET reconstruction strategy, methodology, step-by-step processes and structural variation analysis were previously reported[4]. A movie about IPET antibody reconstruction procedures, including the raw images and intermediate results, 3D density map and structural docking was also available to public by uploaded to YouTube[5]. Comparison of the 3D reconstructions from different individual antibody particles could reveal the protein dynamics and conformational changes during chemical reactions[4,5].

Considering that over 50% of proteins have molecular mass ranging from 40 - 200 kDa[1,2], the success in imaging these small proteins evidenced that OpNS method is a useful tool to push the conventional EM boundary toward small and asymmetric structural determinations and mechanism discoveries. Thus, the detailed protocol is provided as below.

Protocol

1. Preparation of Fresh Negative Staining Solution at 1% (w/v)

1. Put 1 mg Uranyl Formate (UF) powder into glass bottle containing 100 ml deionized water in a dark room or box.
2. Stir the solution O/N at RT in a dark room/box. Wrap the solution bottle with aluminum foil to prevent light from hitting the solution.
3. Filter the solution gently through 0.2 µm (pore size) filter mounted on a 5 ml syringe. The filtered solution was collected into several aluminum foil covered Falcon tubes. The filter syringe must also be wrapped with aluminum foil to prevent light exposure.
4. Filter the solution again through 0.02 µm (pore size) filter mounted on 1 ml syringe. The filtered solution was collected and aliquot into 2 ml vials. The syringes and vials being covered with aluminum foil prior to use.
5. Freeze the aliquot vials using long handled forceps submerging the vials into a liquid nitrogen filled container immediately after the solution was filtered.
6. Transfer the frozen vials into a -80 °C freezer for storage and future usage.

2. Preparation of Negative Staining Workstation and Incubation Workstation

1. Thaw a vial of 1% UF solution in a water bath set at RT. Make sure that the aluminum foil remains wrapped around the vial to prevent exposure to light.
2. Filter the solution after it's completely thawed by using an aluminum foil wrapped 1 ml syringe mounted with a 0.02 µm filter. Collect the filtered solution into a new aluminum foil wrapped vial, and placed it on the ice inside a cap covered ice box waiting for usage.
3. Make solution plates by finger pushing a ~8 inch long Parafilm sheet onto the surface of an empty protein crystallization plate. It will generate rows of circular plates with a diameter of ~5 mm. Make 6 plates in each row place the Parafilm plates on a surface of flattened ice inside an ice container lid, as a staining workstation.
4. Pipette ~35 µl deionized water onto each of left three plates in each row, and pipette ~35 µl filtered UF solution on to right three plates in each row. Cover the staining workstation with a lid to prevent exposure to light before staining proteins.
5. Prepare an EM grid incubation station by filling an empty box halfway with ice, and adhered next to a hanger that can be mounted on a supporting base. Place the sample tweezers in the hanger, in which the tweezers' tips are nearby the ice surface. Half cover the tweezers' tips by the box lip height. An ideal ice box to make an incubation station is using an empty pipet tips container.

3. OpNS Operation

1. Glow-discharge the thin carbon film coated 300 mesh copper EM grids for 10 sec.
2. Pick up a grid with tweezers and hook the tweezers into the hanger by keeping the grid at a 45° tilt and 1 inch above the ice surface inside the incubation station.
3. Dilute the protein sample with Dulbecco's Phosphate Buffered Saline (DBPS) at final protein concentration of ~0.01 to ~0.005 mg/ml. Deposit ~4 µl diluted sample immediately after the dilution on the carbon side of EM grid. (DPBS can be changed to another buffer if the protein is sensitive to DPBS)
4. Incubate the sample on the EM grids for ~1 min inside the incubation station.
5. Remove the excess solution through quickly touching the grid edge with filter paper.
6. Touch the grid quickly to the first drop (~35 µl) of pure water surface atop the Parafilm sheet right after the excess solution was removed on the EM grid. And then remove the excess water promptly with filter paper.
7. Repeat step 3.6 for another two times by washing the EM grid on the remaining two water droplets on the Parafilm (Step 3.6 and 3.7 can be skipped if the sample is very sensitive to water).
8. Float the EM grid immediately on the surface of the first drop of UF solution right after the excess water on the EM grid was removed. And then incubate for 10 sec. Make sure to finish the water washing procedures within 3 sec before floating the grid on the surface of UF solution. The shorter the washing time, the better the quality will be.
9. Clean the tweezers by penetrating the tips into a filter paper for ~2 - 3 times.
10. Remove the excess solution on the grid through contacting the grid edge with the filter paper, and then float the grid on the second drop of UF.
11. Continue above step 3.10 on the second droplet.
12. Float the grid on the third droplet of UF solution and cover the staining station for ~1 min.
13. Optional step: wash the grid quickly on a top of water as described in 3.6. This additional step will benefit samples containing over loaded free gold particles or stain background.
14. Remove the excess solution by touching the filter paper to the entire grid backside (opposite the carbon side). Dry the grid under a gentle stream of nitrogen gas at RT right after observing the solution absorbing to the filter paper.
15. Place the grid onto a sheet of filter paper inside a petri dish, and cover the dish partially with a cap to dry for at least 30 min under RT. For some samples, place the grid in a 40 °C incubator baking for an hr.
16. Store the grid into an EM grid box for future EM examining.

4. EM Examining

1. Align the TEM properly before EM examination of the small proteins on the grid.
    1. Check the resolution of the highest visible Thon-ring that is the power spectrum of an amorphous carbon film to determine whether the TEM has been aligned properly. Since the TEM is shared by many different users, the TEM was often not properly aligned.
    2. Carefully check the power spectrum on the carbon film area of the specimen to adjust the alignment condition of the machine. The highest visible Thon-rings are better than the targeted resolution.
    NOTE: As an example of a proper alignment of a LaB6 filament TEM operated under 120 kV high tension, more than 20 Thon-rings can be visualized, in which, the corresponding resolution can be better than 5.0 Å. This Thon-ring was achieved by Fourier transfer of an amorphous carbon film imaged under a defocus of ~1.6 µm and a dose of 20.4 e-/Å2 (**Figure 5**).
    NOTE: Observation of the high resolution Thon-ring is a necessary condition, but not a sufficient condition for proper alignment. To actually achieve the high resolution images, many other parameters are also important, such as sample quality, radiation damage, charging and drifting as well as the illumination dose rate.

2. Bring the defocus back to near-Scherzer focus for imaging the small proteins on an ideally stained area.
3. Search for "cloudy" area to image. An ideally stained area is usually located near the edge of a thicker stain area, which looks like a "cloudy" area on the grid since the thickness of the stain is normally not evenly distributed on the carbon-coated grid (**Figure 6**). Typically a low magnification (<100x) was to help to find these cloudy areas first before zooming in for imaging.

Representative Results

The implementations of OpNS include the structural and morphological examinations of various lipoprotein species such as: nascent recombinant HDL (rHDL), spherical recombinant HDL, plasma HDL, LDL, IDL and VLDL **(Figure 2)**[30]; as well as small proteins such as 53 kDa CETP (among the smallest proteins successfully imaged through EM) **(Figure 3)**[6] and 160kDa IgG antibodies (one of the most dynamic and heterogeneous proteins) **(Figure 4)**[4,5,29,52], even 28 kDa lipid free apolipoprotein A-1 **(Figure 2L)**, and GroEL and Proteasomes **(Figure 2M** and **N)**.

Other examples of OpNS as a high-throughput method are examining protein#protein interactions for uncovering the protein mechanisms, such as 53 kDa CETP. As described in the introduction, how CETP interacts with different subclasses of lipoproteins were investigated via examining more than 400 EM specimens[6] As far as we know, there was no such a case of cryo-EM study that involves screening nearly a hundred different conditions .

OpNS can expand EM boundaries to study small and asymmetric protein 3D structure and even expand to achieve 3D structure form a single and individual protein (without averaging). For example, IgG antibody is 160 kDa molecule with a highly flexible structure, in which the 3D reconstruction at intermediate resolution is challenging to be achieved. the OpNS method was used to image an individual IgG antibody from a series of tilting angles **(Figure 4E** and **H)**. The reasonably high-resolution and high contrast protein images from OpNS allowed for the successful reconstruction of a single protein by individual particle electron tomography (IPET) **(Figure 4E - J)**[4,5]. In IPET 3D reconstruction[4], the 2D tilt series of the targeted antibody were gradually aligned to their calculated global center via subsequently iterative reconstruction to achieve a 3D density at a resolution of ~14.1 Å **(Figure 4F and G)**[4]. By the same approach, a single antibody#peptide complex was reconstructed, and the peptide induced the internal domain conformational change of a single antibody particle was discovered **(Figure 4I and J**, resolution ~16.6 Å**)**[4,5]. Comparing the 3D reconstructions from different individual particles, the structural analysis may allow us to reveal protein thermodynamic fluctuations, and even “snap-shot” the intermediate stages of a chemical reaction[4,5,29,53,54].

In summary, the proteins with molecular mass between 40 kDa - 200 kDa are challenging for standard EM structural examinations and reconstructions. Considering that over 50% of proteins have molecular mass ranging from 40 - 200 kDa[1,2], we report an OpNS method as a robust and high-throughput tool to push the conventional EM boundary toward small and asymmetric structural determinations and even mechanistic studies.

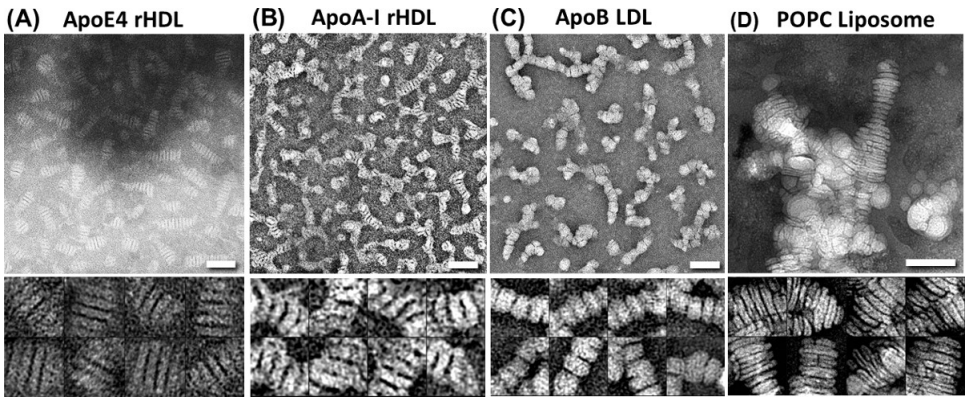

Figure 1. Rouleau artifact of lipoproteins by conventional negative staining (NS) EM. Electron micrographs (above panels) and selected particles (below panels) show various lipoproteins with rouleaux after NS with phosphotungstic acid (PTA) under standard mix procedure. **(A)** Reconstituted HDL (rHDL) with ApoE4, **(B)** apoA-I-containing 9.6 nm discoidal rHDL, **(C)** apoB containing plasma LDL, **(D)** non-apolipoprotein-containing POPC liposomes. Bars: 50 nm. Window size: A and C, 20 nm; B, 30 nm. The Journal of Lipid Research initially published this work[29,30]. Please click here to view a larger version of this figure.

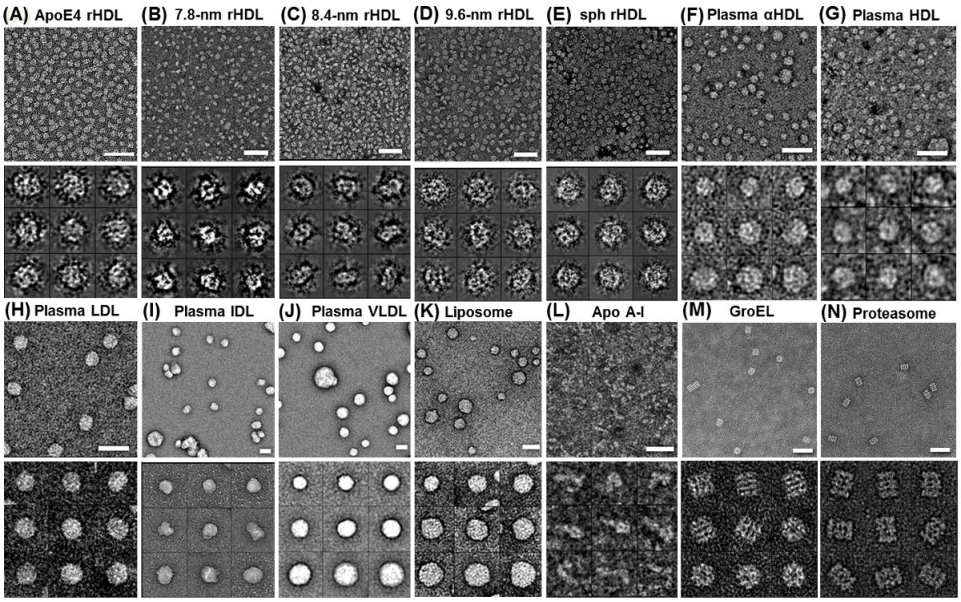

Figure 2. Protein structure by optimized negative staining (OpNS) EM. Electron micrographs show various lipoproteins and liposomes without rouleaux artifact by OpNS. **(A)** apoE4-containing rHDL; **(B)** 7.8 nm rHDL; **(C)** 8.4 nm rHDL; **(D)** 9.6 nm rHDL; **(E)** 9.3 nm spherical rHDL; **(F)** Human plasma α-HDL; **(G)** Plasma HDL; **(H)** Human plasma LDL; **(I)** Human plasma IDL; **(J)** Human plasma VLDL; **(K)** POPC liposome; **(L)** lipid free apoA-I. Additional verification was done using **(M)** GroEL and **(N)** Proteasome samples. Micrographs (above panels) and selected particles (below panels). Bars: 50 nm. Window size: A - D, 20 nm; E and F, 25 nm; G, 20 nm; H, 25 nm; I, 50 nm; J and K, 100 nm; L, 80 nm., Except lipid free apoA-I, GroEL and Proteasome, This research was originally published in the Journal of Lipid Research[29,30]. Please click here to view a larger version of this figure.

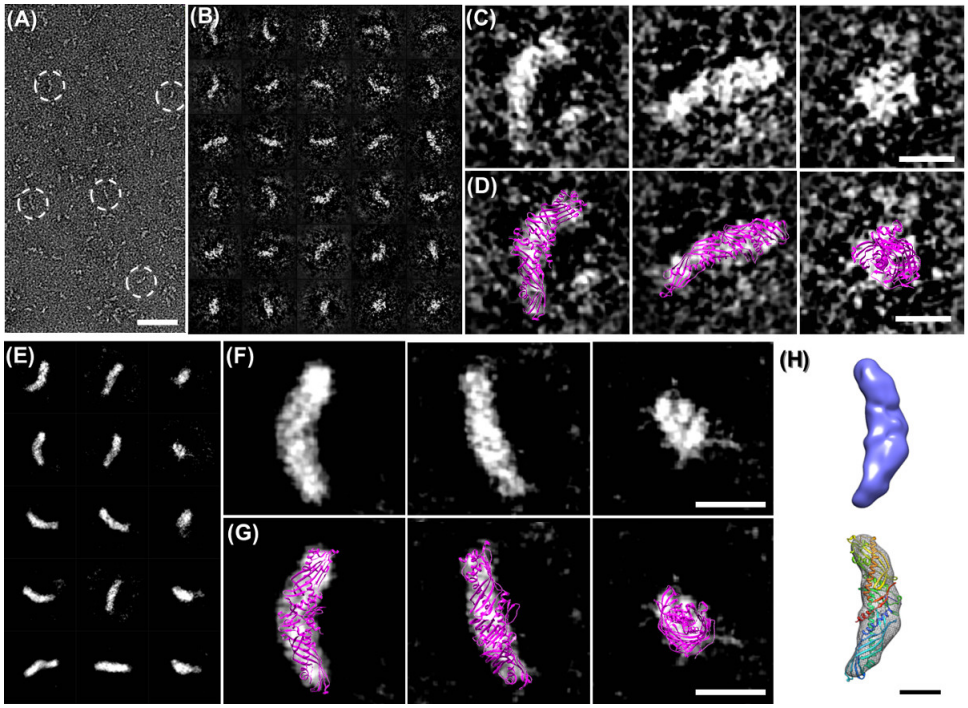

Figure 3. OpNS electron micrographs of CETP. (A) Overview micrograph with CETP (dashed circles) banana shaped particles. **(B)** Windowed select raw particles. **(C)** Three single raw CETP particle images clearly showing a bigger, heavier and larger globular tip including the other smaller, lighter and narrower tip (left panel), top view showing similar terminal regions with less overall curvature (middle panel), and end view down the long axis of CETP (right panel). **(D)** Superimposing the crystal structure (PDB: 2OBD) onto these raw CETP particle images, matches well in both structural shape and domain size showing the orientation can be nearly directly defined even without assistance by computer (corresponding panels to **(C)**). **(E)** Reference free 2D class averages (an *ab initio* process to compute the similarities (cross-correlation calculation) of these randomly oriented particles, the particles having a high similarity to each other were grouped, aligned and then averaged to reduce the background noise and enhanced the particle image contrast. The reference free 2D class averages are calculated by *refine2D.py* software in the EMAN package, in which, no any human made initial model was involved in this class average. The reference class averages can be used as an independent method to validate the 3D reconstruction from single-particle reconstruction). **(F)** Selected reference free 2D class averages show a larger distal end compared to the other. **(G)** Superimposed crystal structure (PDB: 2OBD) comparison to the reference free averages, the overlay images show a near perfect matches between crystal-structure and reference-free class average in both structure shape and domain size (low panel). **(F)** 3D density map of CETP at a resolution of 13 Å was reconstructed from 8,879 particles imaged by OpNS and single-particle reconstruction method (top panel) and the ridged-body docked into this single-particle reconstruction by the crystal structure (low panel). The detailed information of the single particle reconstruction, including image preprocessing, initial model, refinement procedures, angle distribution and Fourier Shell Correlation (FSC) were published in the method section and supporting information of the original paper (H) Final comparison of single particle reconstruction (above panel) and additional PDB fit comparison (bottom panel) [6]. Bars: A, 50 nm; B - D, 10 nm; F, 3 nm. Some of these figures were previously published in the Nature Chemical Biology[6]. Please click here to view a larger version of this figure.

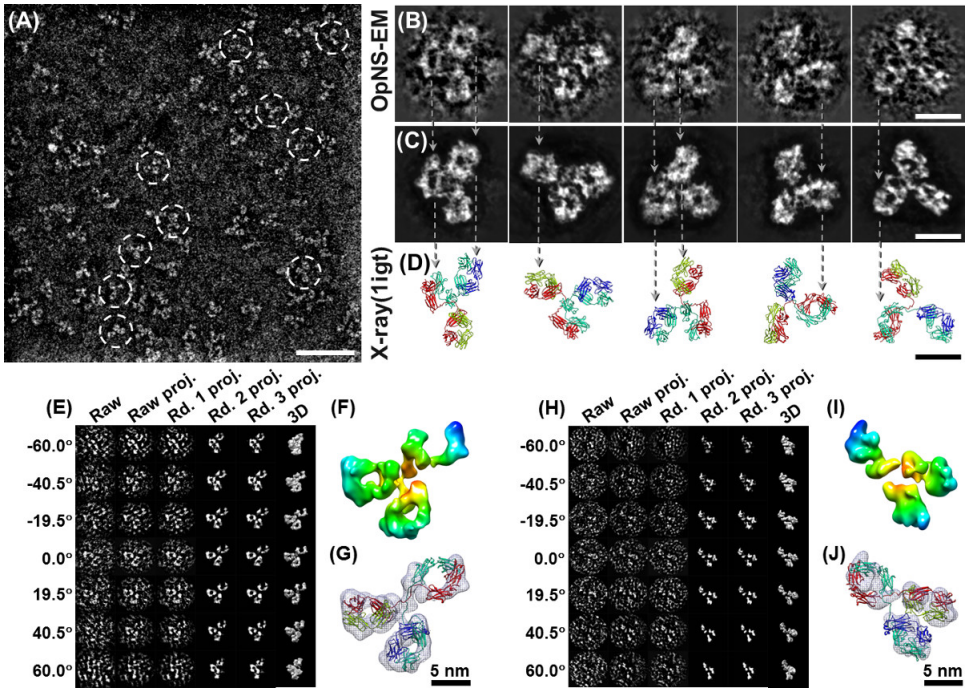

Figure 4. OpNS images and reconstructions of Human IgG1 antibody particles. (A) Overview of human IgG1 antibody OpNS images. Particles shown in white circles clearly display the particles with 3 subdomains. **(B)** Selected high-resolution raw images of five individual unconjugated antibody particles and **(C)** their corresponding noise-reduced images by manually reducing noise surrounding raw particle edge (without touch any density inside the particles) to visualize easily. **(D)** The crystal structure (PDB entry 1IGT) of IgG1 antibody that was oriented to a similarly viewing to the EM images. Comparison of the corresponding images shows many common features between the EM image and the crystal structure, including domain positions and shapes. **(E)** The step-to-step procedure of an *ab initio* 3D reconstruction from a single instance IgG1 antibody (no average, one individual object) using individual#particle electron tomography (IPET) method. **(F)** The final 3D reconstruction of a single antibody particle at resolution of 14.1 Å showed three donut shaped domains forming in a "Y" shape. **(G)** Docking the domains crystal structures into each of corresponding domain density maps respectively, and manually repeating the loops among the domains. **(H)** The step-to-step procedure of 3D reconstruction of a single IgG-peptide complex (no average, one individual object) by IPET. **(I)** The final 3D reconstruction of an IgG peptide complex was displayed at resolution of 16.6 Å showed three rod shaped domains forming in a "Y" shape. **(J)** Respectively, docking the crystal structure of each IgG antibody domains (PDB entry: 1IGT) into each rod shape densities showed a poorly matching with domain crystal structures, suggesting an inner domain conformational change after peptide conjugation. The detailed procedure, resolution analysis and statistics were described in the original paper [5] Bars: A, 50 nm; B - D, 10 nm. This work initially published in PLoS ONE[4] and Scientific Reports[5]. Please click here to view a larger version of this figure.

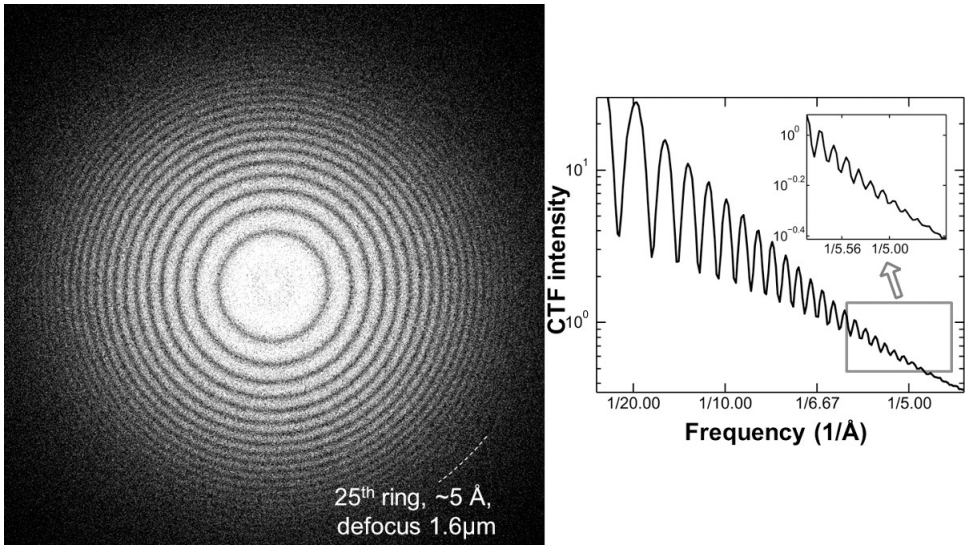

Figure 5. Power spectrum of amorphous carbon film imaged under 1.6 μm defocus by a Zeiss Libra 120 LaB6 TEM. High-resolution imaging requires sufficient evidence to show that EM has the proper alignment and high-resolution capability. The analysis of the power spectrum of nearby carbon area on the grid is an efficient method to check the beam coherence condition prior to data acquisition. Fourier transfer of the image of an amorphous carbon area show the instrument related contrast transfer function (CTF), so called Thon-rings. A proper alignment and coherence can be reflected by the number of visible Thon-rings and the highest resolution of visible Thon rings under a relatively high defocus condition. As an example of a near proper alignment condition of a LaB_6 filament equipped TEM, more than ~20 Thon rings (~5 Å) can be generated from a carbon film are imaged at 1.6 μm defocus using dose 20.4 $e^-/Å^2$. The Thon rings achieved from a low-end TEM have a similar to that from high-end TEM, such as a field-emission gun (FEG) enhanced TEM operated under a proper alignment condition. This work initially published in Scientific Reports[5]. Please click here to view a larger version of this figure.

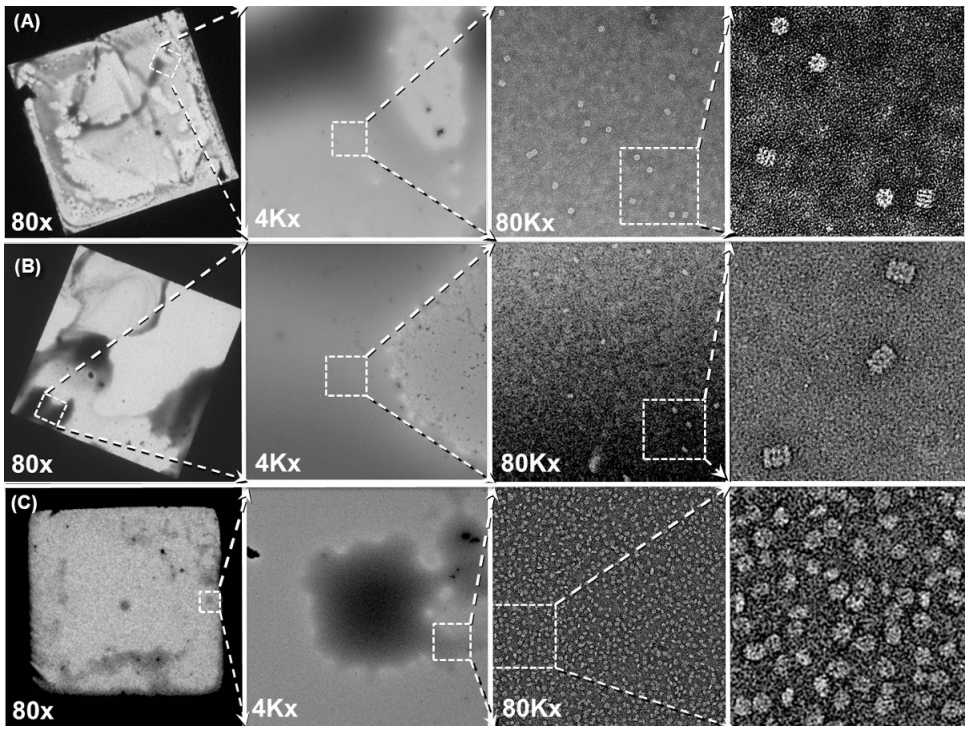

Figure 6. Example micrographs of "ideal" areas for OpNS imaging. Three protein samples, **(A)** GroEL **(B)** Proteasome **(C)** Spherical HDL, were used as examples to demonstrate the ideal OpNS for imaging. Since stains are unevenly distributed in the specimen, the low-magnification of sample usually appears "cloudy" (leftmost panel). The ideal areas for imaging are normally located in the boundaries of these "clouds". An example of step-by-step zoom-in one "cloudy" stain region (left middle panel) show the high-magnification images presenting with high-resolution and high contrast images of particles (right middle panel). Selected images of particles show the structure details of proteins (rightmost panel). Bars: 30nm. Please click here to view a larger version of this figure.

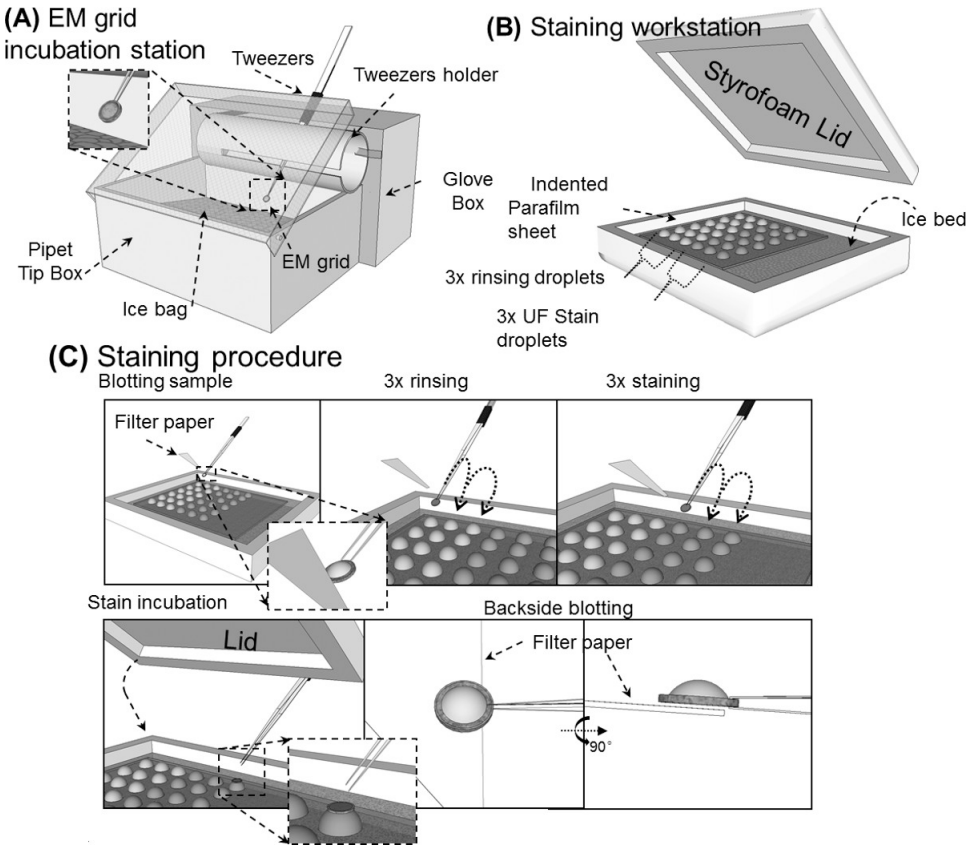

Figure 7. A schematic diagram of OpNS procedures. (A) EM grid incubation station, simple station to incubate the sample solution on the glow-discharged grid. **(B)** Staining workstation, designed to maintain water washing droplets, and stain droplets above an ice bed, while minimizing stain exposure to light. **(C)** Overview of staining procedure, illustrating: blotting direction, 3x water rinsing, 3x UF stain exposure, Staining incubation with inverted sample grid on stain droplets, and final backside sample blotting to ensure a thin layer of sample stain solution prior to drying by nitrogen air. Please click here to view a larger version of this figure.

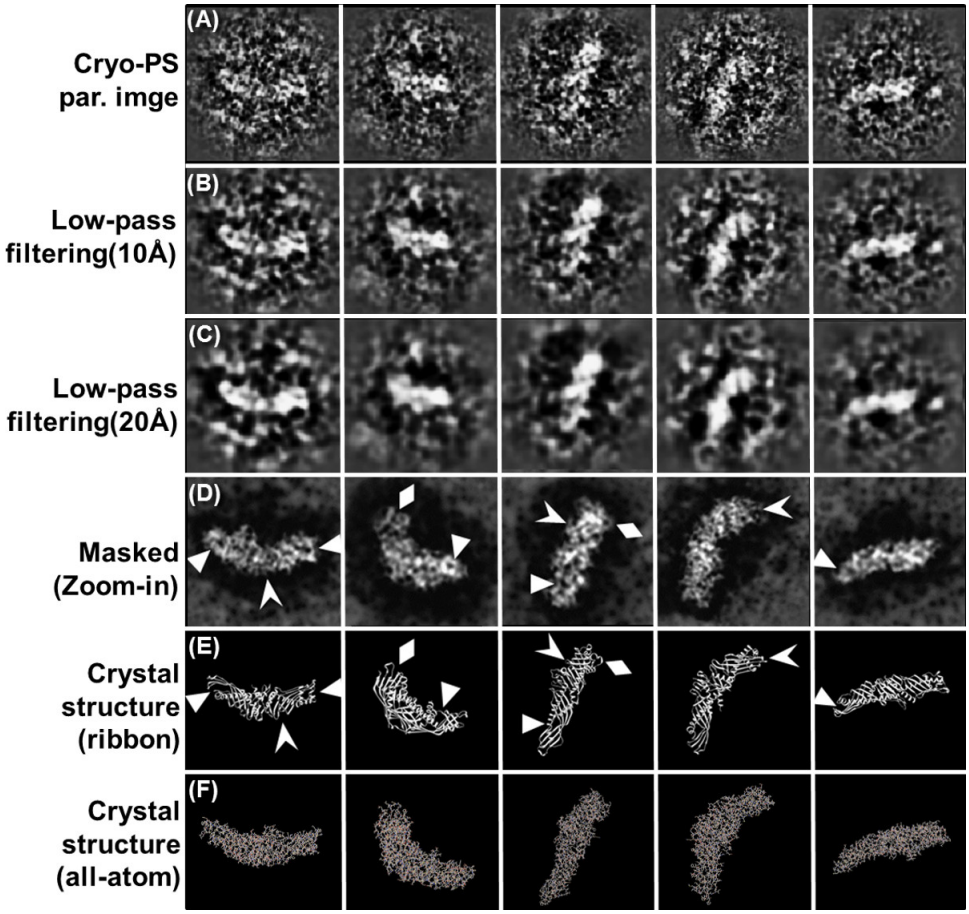

Figure 8. High-resolution images of 53kDa small protein CETP revealed from a modified OpNS method, cryo-positive-staining (cryo-PS). Five select high-resolution and circular shape soft masked raw images of CETP particles (with reverse contrast) and particle shape masked raw particles (manually reduced noise surrounding raw particle images' edges, but without modifying any density within the particles) to visualize easily. All-atom and ribbon crystal structure comparison to masked raw particles aligned to similar orientations of each particle to EM images. The high-resolution details of the raw image areas display certain similarity with the crystal structure, while not all crystal structure features can be resolved from raw data. Remarkably, these raw images show similarity in both terminal ends having nearby small circular holes seen in manually reduced noise images (triangles); moreover, the strands in the C-terminal regions within particle images complement crystal structure β-sheets (arrows) and finally, protruding loops on the CETP C-terminal region are akin to in the crystal structure (diamonds). **(A)** Five select high-resolution and circular shape soft masked raw images of CETP particles (with reverse contrast). **(B)** Low pass filtering to 10Å. **(C)** Higher Low pass filtering to 20Å. **(D)** Masked manually noise reduced images. **(E)** Crystal structure comparison by ribbon structure. **(F)** Crystal structure comparison by all atom representation. Bar: 5nm. Part of this work was published in Nature Chemical Biology[6]. Please click here to view a larger version of this figure.

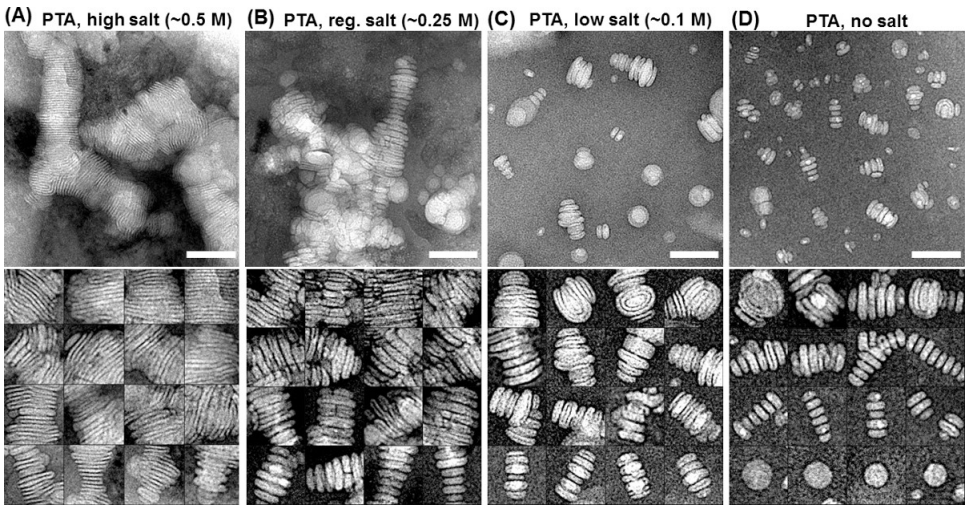

Figure 9. Electron micrographs of liposomes showing rouleau formation by conventional NS protocol (PTA stain) under differing salinity. (A) High salinity (~0.5 MNaCl). **(B)** Regular salinity (~0.25 M NaCl). **(C)** Low salinity (~0.1 M NaCl). **(D)** Pure water. Micrographs (above panel) and select windowed particles (below panel) shown. Bars: 100 nm. Window size: 80 nm. The Journal of Lipid Research originally published this work[30]. Please click here to view a larger version of this figure.

Discussion

Compared to conventional NS techniques, OpNS can prevent rouleaux artifacts (**Figure 1** and **9**), providing reliable and reasonable high# resolution (~1nm) structural details of small proteins (**Figure 2**). Compared to cryo-EM, OpNS provides a high throughput method and can examine a wide variety of proteins and protein-protein interactions[6]. However, OpNS still has its disadvantages. Compared to conventional NS, OpNS entails: i) more complicated steps in specimen preparation; ii) using a radioactive substance, UF; iii) keeping the stain fresh due to the shorter potency of the UF stain because of its light sensitivity; iv) to prevent precipitation the UF solution must be stored in -80 °C and requires thawing before use; v) and finally all UF must be handled as hazardous waste. Compared to cryo-EM, OpNS provides relatively lower resolution images and no guarantee for any not yet discovered artifact in future.

NS operation procedural effects on lipoprotein rouleaux formation

NS protocols for preparing proteins for examination[16,29-36,55] can be classified into three major groups of methods[50]: mixing[55], drop-by-drop[16], and washing procedures[29]. i) The mixing protocol requires the preliminary mixing of the stain and protein sample at a specific ratio, and then applying the mixed solution onto carbon film coated on a grid, finally removing excess solution with filter paper before air drying for EM examination[55]. ii) The drop#by#drop protocol involves applying (~4 µl) sample drop directly to an EM grid coated in carbon letting sit for ~1 min, subsequently removing excess sample solution before application of a drop (~4 µl) of stain solution on the same side of grid. After ~1 min of incubation, remove the excess stain through contact with clean filter paper, finally submitting for air drying[16,56-58]. iii) The washing protocol (**Figure 7**) requiring sample solution application to an EM grid coated in carbon for 1 min, then washing with deionized water three times right after removing the excess solution each time by filter paper[3,29,30]. OpNS protocol was modified from this washing procedure.

NS stain types and effects on lipoprotein rouleaux formation

In NS, stronger electron scattering due to heavy metal stains provide contrast from the proteins[17-20,59]. NS samples can additionally suffer greater radiation doses, and enhance protein features by a sharper negative contrast[8,9,60]. Stains of heavy metals can be classified as: anionic, including phosphotungstic acid (PTA)[16], methylamine tungstate[14] and silicon tungstate[61]; and cationic, such as Uranyl acetate (UA)[62], UF[3,29,30], and Uranyl nitrate (UN)[63]. One of the anionic NS stains that is most commonly used is PTA[33,64-67]. PTA is a heteropoly acid, which is typically used around a pH 7.0 - 7.5. PTA can also be used for positive staining[3,16,68]. The negative charges of PTA may mediate electrostatic interactions with unsaturated lipids positively charged head groups, like POPC, on both lipoprotein and liposome surfaces. PTA may cause rouleaux formation through this interaction [29,30] even under regular buffer salinity[29,30] (**Figure 1**). Uranyl stains, such as UA, UF and UN are alternative choices for cationic heavy metals stains and UA in particular is frequently used for NS of a variety of biological specimens[62,69,70]. Experiments found UF causes no rouleaux of lipoproteins that contain unsaturated fat acid lipids, such as POPC. However, UF may still induce rouleaux formation on lipoprotein that contain saturated fatty acid lipids, such as the dimyristoyl phosphatidylcholine (DMPC) and 1-hexadecanoyl-2-octadecanoyl-sn-glycero-3-phosphocholine (PSPC). The detailed mechanism of this interaction is unknown. UA/UF/UN can all work at lower pH values ranging from 3.5 to 4.6. Such lower pH values may not suitable for certain biological macromolecules that are sensitive to pH[14,71]. Interestingly, UA/UF can fix protein structure within a few milliseconds through an unknown mechanism[72]. Unlike PTA, UA/UF is more similar to a salt than an acid.

UF reportedly can provide better results than UA[73], in which, UF and UN stains have smaller grain sizes than UA (UF: 0.3 nm, UN: ~0.5 nm)[3,74]. An interesting example, secondary structure-like details of a small protein (53 kDa CETP) can be directly visualized from the raw micrographs when UF was used as negative-stain reagent by following the earlier reported cryo-positive-staining (cryo-PS) method (**Figure 8**)[6]. In cryo-PS, the stained sample was flash frozen by following cryo-EM sample preparation procedure instead of drying procedure in OpNS protocol, which may cause the secondary structural collapse. The cryo-PS is a method for high-contrast and high-resolution imaging of small proteins[75]. Since the cryo-PS images have reversed contrast compared to those from the reported cryo-NS protocol [22], but have consistent image contrast to those from conventional cryo-EM images, thus it was named the cryo-PS method. The cryo-PS images show that the staining reagent, Uranyl formate, penetrates the molecular surface, challenging the conventional view that staining can visualize only the outer surface structure. The

mechanism of how Uranyl formate penetrates the molecular surface is unknown. One possibility is that the Uranyl cation binds available protein carboxyl groups, and thus the surrounding vitreous ice is of lower density than the staining of the protein and Uranyl groups, thereby acting as a positive stain. The cryo-PS method is similar to multiple isomorphous replacement (MIR) method, which was a common approach to solve the phase problem in X-ray crystallography [76-78]. In MIR, crystal samples are soaked with a heavy atom solution, including Uranium, to get an isomorphic form to its native form. The addition of the heavy atom sometimes does not affect the crystal formation or unit cell dimensions but provides additional information of crystal structure determination[76-78]. By benefiting from the small grain of UF, cryo-PS could provide a high contrast and high-resolution image of a single protein, which is important for protein structure studies, especially when considering that nearly all proteins are naturally dynamic and heterogeneous in solution. For validation of this cryo-PS method, we open for any blind test from the EM field.

Salt concentration effects on the rouleaux formation in lipoproteins

Using traditional PTA negative staining reagent, observed rouleaux formation is more likely related to lipid interactions instead of protein interaction. Imaging the samples of POPC liposome vesicles prepared under considerable salinity (0.5 M NaCl), moderate salinity (0.25 M NaCl), relatively weak salinity (0.1M NaCl), and pure water (**Figure 9**), the electron micrographs show the rouleaux formation was correlated to salt concentration (**Figure 9A** - **D**). Using UF as negative staining reagent, no rouleaux was observed in POPC liposome vesicle sample[30] (**Figure 2L**), suggesting the washing procedure to quickly reduce the salt concentration right before staining is an necessary, but not independently sufficient step for preventing rouleaux in POPC related samples.

TEM imaging small protein requires a near-Scherzer focus condition.

Successful TEM imaging of small proteins at higher resolution requires two critical conditions, a proper beam alignment and a near-Scherzer focus acquisition condition. i) A proper beam alignment can be judged through the number of visible Thon rings (power spectrum) on the Fourier transfer of a carbon film image acquired under a relatively high defocus. The better the alignment condition of the beam, the more Thon rings can be visualized and measurable.. ii) Acquiring image under a near-Scherzer focus is another critical condition. A traditional standard strategy for imaging biological specimens typically utilizes high defocus (1 - 2 µm and even more), which can enhance the biological sample image contrast [79]. This strategy is significant different from the typical strategy for imaging atomic resolution structure of hard materials, which often utilizes a near Scherzer focus (~50 nm defocus). Although, a higher defocus could strengthen biological sample contrast, high-resolution signals would be partially eliminated. As a result, the complicity of high-resolution signal would be lower at a higher defocus imaging condition. The reason is that, the TEM image is the convolution of sample structure and the instrument CTF. The CTF is an oscillating curve against the frequency, in which the curve frequently oscillated crossing zero amplitude at high frequency. Every time when CTF across zero, the sample structural signal at this specific frequency will be eliminated (zero times any number will be zero). The eliminated signal at this frequency can never be recovered by any CTF correction algorithm (a zero divided by a zero can be any random number instead of the original structural signal). Under higher defocus imaging, the CTF will oscillate much more aggressively, thus the CTF crosses zero amplitude more frequently, as a result, the structural signals at a greater number of specific frequencies will be eliminated. The more signals that are eliminated, the less complicity the image will have. Notably, the complicity of image cannot be recovered or corrected by any CTF correction. However, a number of incompleted images acquired under different defocuses can be used to fill their gaps to each other to obtained a completed structural signal of the sample structure via an averaging method, in which even an atomic resolution can be achieved [9-12] .

The averaging method is a powerful approach to achieve the structure of some highly symmetric proteins and structurally related rigid proteins. However, it still remains challenging in the structural study of small and asymmetric proteins, especially for structural dynamics and flexible proteins, such as antibodies and HDLs. Averaging is based on the assumption that protein particles are identical in structure and conformation but different in orientations, however many proteins are known to undergo thermodynamic fluctuation in solution. By applying the averaging method without previously knowing the protein thermodynamic fluctuation fluctuations, the averaged structure can often cause missing domains [10,80] or local variation in resolution [81] in cryo-EM reconstructions .

The success in achieving the 3D reconstruction of small protein, such as 53 kDa CETP, and 3D structure of a single protein, such as 160 kDa IgG1 antibody, benefits from using the near-Scherzer focus imaging condition under a proper alignment condition. Although the image contrast seems low in the near-Scherzer focus images, the contrast can be easily enhanced by simply applying a low pass filtering to reduce the high-frequency noise in the background. We believe, the near-Scherzer focus images carry the maximum structural signals, and can increase the accuracy of particle alignment and enhance efficiency in single-particle 3D reconstruction and individual particle electron tomography reconstruction.

Disclosures

We have nothing to disclose.

Acknowledgements

We thank Dr. Mickey Yang for editing and comments, and Drs. Lei Zhang and Bo Peng for assistance. This work was supported by the Office of Science, Office of Basic Energy Sciences of the United States Department of Energy (contract no. DE-AC02-05CH11231), the National Heart, Lung, And Blood Institute of the National Institutes of Health (no. R01HL115153), and the National Institute of General Medical Sciences of the National Institutes of Health (no. R01GM104427).

References

1. Lipman, D. J., Souvorov, A., Koonin, E. V., Panchenko, A. R., & Tatusova, T. A. The relationship of protein conservation and sequence length. *BMC Evol Biol.* **2**, 20 (2002).

2. Tran, J. C. *et al*. Mapping intact protein isoforms in discovery mode using top-down proteomics. *Nature.* **480**, 254-258, doi:10.1038/nature10575 (2011).
3. Ohi, M., Li, Y., Cheng, Y., & Walz, T. Negative Staining and Image Classification - Powerful Tools in Modern Electron Microscopy. *Biol Proced Online.* **6**, 23-34 (2004).
4. Zhang, L., & Ren, G. IPET and FETR: experimental approach for studying molecular structure dynamics by cryo-electron tomography of a single-molecule structure. *PLoS ONE.* **7**, e30249, doi:10.1371/journal.pone.0030249 (2012).
5. Tong, H. *et al*. Peptide-conjugation induced conformational changes in human IgG1 observed by optimized negative-staining and individual-particle electron tomography. *Sci Rep.* **3**, 1089, doi:10.1038/srep01089 (2013).
6. Zhang, L. *et al.* Structural basis of transfer between lipoproteins by cholesteryl ester transfer protein. *Nat Chem Biol.* **8**, 342-349, doi:10.1038/nchembio.796 (2012).
7. Henderson, R. Realizing the potential of electron cryo-microscopy. *Q Rev Biophys.* **37**, 3-13 (2004).
8. Sander, B., & Golas, M. M. Visualization of bionanostructures using transmission electron microscopical techniques. *Microsc Res Tech.* **74**, 642-663, doi:10.1002/jemt.20963 (2011).
9. Liu, H. *et al.* Atomic structure of human adenovirus by cryo-EM reveals interactions among protein networks. *Science.* **329**, 1038-1043, doi:10.1126/science.1187433 (2010).
10. Liao, M., Cao, E., Julius, D., & Cheng, Y. Structure of the TRPV1 ion channel determined by electron cryo-microscopy. *Nature.* **504**, 107-112, doi:10.1038/nature12822 (2013).
11. Baker, M. L. *et al.* Validated near-atomic resolution structure of bacteriophage epsilon15 derived from cryo-EM and modeling. *Proceedings of the National Academy of Sciences of the United States of America.* **110**, 12301-12306, doi:10.1073/pnas.1309947110 (2013).
12. Bai, X. C., Fernandez, I. S., McMullan, G., & Scheres, S. H. Ribosome structures to near-atomic resolution from thirty thousand cryo-EM particles. *eLife.* **2**, e00461, doi:10.7554/eLife.00461 (2013).
13. Ren, G. *et al.* Model of human low-density lipoprotein and bound receptor based on cryoEM. *Proc Natl Acad Sci U S A.* **107**, 1059-1064, doi:10.1073/pnas.0908004107 (2010).
14. Bremer, A., Henn, C., Engel, A., Baumeister, W., & Aebi, U. Has negative staining still a place in biomacromolecular electron microscopy? *Ultramicroscopy.* **46**, 85-111 (1992).
15. Brenner, S., & Horne, R. W. A negative staining method for high resolution electron microscopy of viruses. *Biochim Biophys Acta.* **34**, 103-110 (1959).
16. Forte, T. M., & Nordhausen, R. W. Electron microscopy of negatively stained lipoproteins. *Methods in enzymology.* **128**, 442-457 (1986).
17. Colliex, C., *et al*. *International Tables For Crystallography Vol. C.* (ed E Prince) Ch. 4.3, 259-429 Kluwer Academic Publishers (2006).
18. Ren, G, Zuo, J. M., & L.-M, P. Accurate Measurements of Crystal Structure Factors Using a FEG Electron Microscope Using Digital Micrographs. *Micron.* **28**, 459-467 (1997).
19. Peng, L. M., Ren, G., Dudarev, S. L., & Whelan, M. J. Robust parameterization of elastic and absorptive electron atomic scattering factors. *Acta Crystallographica Section A.* **52**, 257-276 (1996).
20. Peng, L. M., Ren, G., Dudarev, S. L., & Whelan, M. J. Debye-Waller factors and absorptive scattering factors of elemental crystals. *Acta Crystallographica Section A.* **52**, 456-470 (1996).
21. Melchior, V., Hollingshead, C. J., & Cahoon, M. E. Stacking in Lipid Vesicle Tubulin Mixtures Is an Artifact of Negative Staining. *Journal of Cell Biology.* **86**, 881-884, doi:10.1083/jcb.86.3.881 (1980).
22. De Carlo, S., & Harris, J. R. Negative staining and cryo-negative staining of macromolecules and viruses for TEM. *Micron.* **42**, 117-131, doi:10.1016/j.micron.2010.06.003 (2011).
23. Allan, V., & Vale, R. Movement of Membrane Tubules Along Microtubules *In Vitro* - Evidence for Specialized Sites of Motor Attachment. *Journal of Cell Science.* **107**, 1885-1897 (1994).
24. Catte, A. *et al.* Novel changes in discoidal high density lipoprotein morphology: a molecular dynamics study. *Biophys J.* **90**, 4345-4360, doi:10.1529/biophysj.105.071456 (2006).
25. Forester, G. P., Tall, A. R., Bisgaier, C. L., & Glickman, R. M. Rat intestine secretes spherical high density lipoproteins. *J Biol Chem.* **258**, 5938-5943 (1983).
26. Gantz, D. L., Walsh, M. T., & Small, D. M. Morphology of sodium deoxycholate-solubilized apolipoprotein B-100 using negative stain and vitreous ice electron microscopy. *Journal of Lipid Research.* **41**, 1464-1472 (2000).
27. Pentikainen, M. O., Lehtonen, E. M., & Kovanen, P. T. Aggregation and fusion of modified low density lipoprotein. *J Lipid Res.* **37**, 2638-2649 (1996).
28. Tall, A. R., Green, P. H., Glickman, R. M., & Riley, J. W. Metabolic fate of chylomicron phospholipids and apoproteins in the rat. *J Clin Invest.* **64**, 977-989, doi:10.1172/JCI109564 (1979).
29. Zhang, L. *et al.* An optimized negative-staining protocol of electron microscopy for apoE4 POPC lipoprotein. *J Lipid Res.* **51**, 1228-1236, doi:10.1194/jlr.D002493 (2010).
30. Zhang, L. *et al.* Morphology and structure of lipoproteins revealed by an optimized negative-staining protocol of electron microscopy. *J Lipid Res.* **52**, 175-184, doi:10.1194/jlr.D010959 (2011).
31. Gong, E. L. *et al.* Discoidal complexes containing apolipoprotein E and their transformation by lecithin-cholesterol acyltransferase. *Biochim Biophys Acta.* **1006**, 317-328 (1989).
32. Schneeweis, L. A., Koppaka, V., Lund-Katz, S., Phillips, M. C., & Axelsen, P. H. Structural analysis of lipoprotein E particles. *Biochemistry.* **44**, 12525-12534, doi:10.1021/bi050872j (2005).
33. Raussens, V. *et al*. Orientation and mode of lipid-binding interaction of human apolipoprotein E C-terminal domain. *Biochem J.* **387**, 747-754, doi:10.1042/BJ20041536 (2005).
34. Li, X., Kan, H. Y., Lavrentiadou, S., Krieger, M., & Zannis, V. Reconstituted discoidal ApoE-phospholipid particles are ligands for the scavenger receptor BI. The amino-terminal 1-165 domain of ApoE suffices for receptor binding. *J Biol Chem.* **277**, 21149-21157, doi:10.1074/jbc.M200658200 (2002).
35. Innerarity, T. L., Pitas, R. E., & Mahley, R. W. Binding of arginine-rich (E) apoprotein after recombination with phospholipid vesicles to the low density lipoprotein receptors of fibroblasts. *J Biol Chem.* **254**, 4186-4190 (1979).
36. Lu, B., Morrow, J. A., & Weisgraber, K. H. Conformational reorganization of the four-helix bundle of human apolipoprotein E in binding to phospholipid. *J Biol Chem.* **275**, 20775-20781, doi:10.1074/jbc.M003508200 (2000).
37. Antwerpen, R., La Belle, M., Navratilova, E., & Krauss, R. M. Structural heterogeneity of apoB-containing serum lipoproteins visualized using cryo-electron microscopy. *J Lipid Res.* **40**, 1827-1836 (1999).

38. Antwerpen, R. *et al.* Cryo-electron microscopy of low density lipoprotein and reconstituted discoidal high density lipoprotein: imaging of the apolipoprotein moiety. *J Lipid Res.* **38**, 659-669 (1997).
39. Silva, R. A. *et al.* Structure of apolipoprotein A-I in spherical high density lipoproteins of different sizes. *Proc Natl Acad Sci U S A.* **105**, 12176-12181, doi:10.1073/pnas.0803626105 (2008).
40. Antwerpen, R. Preferred orientations of LDL in vitreous ice indicate a discoid shape of the lipoprotein particle. *Arch Biochem Biophys.* **432**, 122-127 (2004).
41. Davidson, W. S., & Silva, R. A. Apolipoprotein structural organization in high density lipoproteins: belts, bundles, hinges and hairpins. *Curr Opin Lipidol.* **16**, 295-300 (2005).
42. Peters-Libeu, C. A., Newhouse, Y., Hatters, D. M., & Weisgraber, K. H. Model of biologically active apolipoprotein E bound to dipalmitoylphosphatidylcholine. *J Biol Chem.* **281**, 1073-1079 (2006).
43. Peng, D. C., Song, C., Reardon, C. A., Liao, S. S., & Getz, G. S. Lipoproteins produced by ApoE-/- astrocytes infected with adenovirus expressing human ApoE. *Journal of Neurochemistry.* **86**, 1391-1402, doi:DOI 10.1046/j.1471-4159.2003.01950.x (2003).
44. Peters-Libeu, C. A., Newhouse, Y., Hall, S. C., Witkowska, H. E., & Weisgraber, K. H. Apolipoprotein E*dipalmitoylphosphatidylcholine particles are ellipsoidal in solution. *J Lipid Res.* **48**, 1035-1044, doi:10.1194/jlr.M600545-JLR200 (2007).
45. Jones, M. K. *et al.* Assessment of the validity of the double superhelix model for reconstituted high density lipoproteins: a combined computational-experimental approach. *J Biol Chem.* **285**, 41161-41171, doi:10.1074/jbc.M110.187799 (2010).
46. Carnemolla, R. *et al.* The specific amino acid sequence between helices 7 and 8 influences the binding specificity of human apolipoprotein A-I for high density lipoprotein (HDL) subclasses: a potential for HDL preferential generation. *J Biol Chem.* **283**, 15779-15788, doi:10.1074/jbc.M710244200 (2008).
47. Sivashanmugam, A. *et al*. Structural basis of human high-density lipoprotein formation and assembly at sub nanometer resolution. *Methods Cell Biol.* **90**, 327-364, doi:10.1016/S0091-679X(08)00815-7 (2008).
48. Cavigiolio, G. *et al.* The interplay between size, morphology, stability, and functionality of high-density lipoprotein subclasses. *Biochemistry.* **47**, 4770-4779 (2008).
49. Chen, B. *et al*. Apolipoprotein AI tertiary structures determine stability and phospholipid-binding activity of discoidal high-density lipoprotein particles of different sizes. *Protein Sci.* **18**, 921-935, doi:10.1002/pro.101 (2009).
50. Zhang, L., Tong, H., Garewal, M., & Ren, G. Optimized negative-staining electron microscopy for lipoprotein studies. *Biochim Biophys Acta.* **1830**, 2150-2159, doi:10.1016/j.bbagen.2012.09.016 (2013).
51. Tong, H. M., Zhang, L., Huang, L. Q., & Ren, G. Optimized negative-staining protocol for electron microscopy study of lipoprotein structure. *Progress in Biochemistry and Biophysics.* **39**, 972-978, doi:Doi 10.3724/Sp.J.1206.2012.00224 (2012).
52. Zhang, L., Kaspar, A., Woodnutt, G., & Ren, G. Monitoring the Structural Changes of Conjugated Antibodies by High-Resolution Electron Microscopy and Individual-Particle Electron Tomography. *Biophysical Journal.* **98**, 440a-441a (2010).
53. Ren, G., & Zhang, L. Asymmetric Small Protein Structure Determination by Individual Particle Electron Tomography. *Biophysical journal.* **102**, 394a, doi:10.1016/j.bpj.2011.11.2153 (2012).
54. Zhang, L., & Ren, G. Structural Determination of Heterogeneous Protein by Individual-Particle Electron Tomography - Combination of Electron Tomography and Local Refinement Reconstruction Method for High-Resolution Structural Determination of Each Individual Protein Particle. *Biophysical journal.* **98**, 441a, doi:10.1016/j.bpj.2009.12.2394 (2010).
55. Forte, T., Norum, K. R., Glomset, J. A., & Nichols, A. V. Plasma lipoproteins in familial lecithin: cholesterol acyltransferase deficiency: structure of low and high density lipoproteins as revealed by elctron microscopy. *J Clin Invest.* **50**, 1141-1148 (1971).
56. Fang, Y., Gursky, O., & Atkinson, D. Lipid-binding studies of human apolipoprotein A-I and its terminally truncated mutants. *Biochemistry.* **42**, 13260-13268 (2003).
57. Gursky, O., Ranjana & Gantz, D. L. Complex of human apolipoprotein C-1 with phospholipid: thermodynamic or kinetic stability? *Biochemistry.* **41**, 7373-7384, doi:10.1021/bi025588w (2002).
58. Jayaraman, S., Gantz, D. L., & Gursky, O. Effects of protein oxidation on the structure and stability of model discoidal high-density lipoproteins. *Biochemistry.* **47**, 3875-3882, doi:10.1021/bi7023783 (2008).
59. Ren, G., & Peng, L. M. The Analytic Doyle-Turner Representation of High Energy Electron Absorptive Structure Factors. *Acta Physica Sinica.* **45**, 1344-1349 (1996).
60. Ren, G., Reddy, V. S., Cheng, A., Melnyk, P., & Mitra, A. K. Visualization of a water-selective pore by electron crystallography in vitreous ice. *Proc Natl Acad Sci U S A.* **98**, 1398-1403, doi:10.1073/pnas.041489198 (2001).
61. Camejo, G., Suarez, Z. M., & Munoz, V. The apo-lipoproteins of human plasma high density lipoprotein: a study of their lipid binding capacity and interaction with lipid monolayers. *Biochim Biophys Acta.* **218**, 155-166 (1970).
62. Kondo, A., Muranaka, Y., Ohta, I., & Kanno, T. Dynamic reaction in a homogeneous HDL-cholesterol assay visualized by electron microscopy. *Clin Chem.* **45**, 1974-1980 (1999).
63. Tufteland, M., Ren, G., & Ryan, R. O. Nanodisks derived from amphotericin B lipid complex. *J Pharm Sci.* **97**, 4425-4432, doi:10.1002/jps.21325 (2008).
64. Clay, M. A., Pyle, D. H., Rye, K. A., & Barter, P. J. Formation of spherical, reconstituted high density lipoproteins containing both apolipoproteins A-I and A-II is mediated by lecithin : cholesterol acyltransferase. *Journal of Biological Chemistry.* **275**, 9019-9025, doi:10.1074/jbc.275.12.9019 (2000).
65. Desilva, H. V., Masoliva, J., Taylor, J. M., & Mahley, R. W. Identification of Apolipoprotein B-100 Low-Density Lipoproteins, Apolipoprotein B-48 Remnants, and Apolipoprotein E-Rich High-Density-Lipoproteins in the Mouse. *Journal of Lipid Research.* **35**, 1297-1310 (1994).
66. Fagan, A. M. *et al.* Unique lipoproteins secreted by primary astrocytes from wild type, apoE (-/-), and human apoE transgenic mice. *Journal of Biological Chemistry.* **274**, 30001-30007, doi:10.1074/jbc.274.42.30001 (1999).
67. Musliner, T. A. *et al*. Dissociation of high density lipoprotein precursors from apolipoprotein B-containing lipoproteins in the presence of unesterified fatty acids and a source of apolipoprotein A-I. *J Lipid Res.* **32**, 917-933 (1991).
68. Silverman, L., & Glick, D. The reactivity and staining of tissue proteins with phosphotungstic acid. *J Cell Biol.* **40**, 761-767 (1969).
69. Hamilton, R. L., Williams, M. C., Fielding, C. J., & Havel, R. J. Discoidal bilayer structure of nascent high density lipoproteins from perfused rat liver. *J Clin Invest.* **58**, 667-680 (1976).
70. Pollard, H., Scanu, A. M., & Taylor, E. W. On the geometrical arrangement of the protein subunits of human serum low-density lipoprotein: evidence for a dodecahedral model. *Proc Natl Acad Sci U S A.* **64**, 304-310 (1969).
71. Frasca, J. M., & Parks, V. R. A Routine Technique for Double-Staining Ultrathin Sections Using Uranyl and Lead Salts. *J Cell Biol.* **25**, 157-161 (1965).

72. Zhao, F. Q., & Craig, R. Capturing time-resolved changes in molecular structure by negative staining. *Journal of structural biology.* **141**, 43-52 (2003).
73. Knight, D. P. Negative staining of rat tail tendon collagen fibrils with uranyl formate. *Tissue Cell.* **7**, 651-654 (1975).
74. Dash, S. *et al.* Temperature programmed decomposition of uranyl nitrate hexahydrate. *Journal of Nuclear Materials.* **264**, 271-282, doi:10.1016/s0022-3115(98)00495-4 (1999).
75. Zhang, L. *et al*. Structural basis of transfer between lipoproteins by cholesteryl ester transfer protein. *Nature Chemical Biology.* **8**, 342-349, doi:10.1038/nchembio.796 (2012).
76. Kartha, G. Combination of multiple isomorphous replacement and anomalous dispersion data for protein structure determination. 3. Refinement of heavy atom positions by the least-squares method. *Acta crystallographica.* **19**, 883-885 (1965).
77. Kartha, G., & Parthasarathy, R. Combination of Multiple Isomorphous Replacement and Anomalous Dispersion Data for Protein Structure Determination. I. Determination of Heavy-Atom Positions in Protein Derivatives. *Acta crystallographica.* **18**, 745-749 (1965).
78. Kartha, G., & Parthasarathy, R. Combination of Multiple Isomorphous Replacement and Anomalous Dispersion Data for Protein Structure Determination. Ii. Correlation of the Heavy-Atom Positions in Different Isomorphous Protein Crystals. *Acta crystallographica.* **18**, 749-753 (1965).
79. Taylor, K. A., & Glaeser, R. M. Electron microscopy of frozen hydrated biological specimens. *Journal of ultrastructure research.* **55**, 448-456 (1976).
80. Correia, I. *et al*. The structure of dual-variable-domain immunoglobulin molecules alone and bound to antigen. *mAbs.* **5** (2013).
81. Cardone, G., Heymann, J. B., & Steven, A. C. One number does not fit all: mapping local variations in resolution in cryo-EM reconstructions. *Journal of structural biology.* **184**, 226-236, doi:10.1016/j.jsb.2013.08.002 (2013).